Stiffening near-net-shape functional parts of Inconel 718 LPBF considering material anisotropy and subsequent machining issues

José David Pérez-Ruiz [*], Felipe Marin, Silvia Martínez, Aitzol Lamikiz, Gorka Urbikain, Luis Norberto López de Lacalle

Universidad del País vasco, Bilbao, Spain
Centro de Fabricación Avanzada Aeronáutica, CFAA, Zamudio, Spain

ARTICLE INFO

ABSTRACT

Additive manufacturing of metallic parts has witnessed significant development. The laser powder bed fusion (LPBF) process has emerged as a key process for manufacturing thin-walled components. However, despite the significant advances, post-machining operations are required for the improvement of dimensional and surface quality, specifically in low stiffness components. This study proposed an iterative design methodology for improving the stiffness of such LPBF components. In the first stage, an initial assessment of the machining conditions was performed to obtain a first approach to the relationship between tooth passing, natural, and chatter frequencies. Thereafter, a method to improve Young's modulus was proposed by evaluating the elastic anisotropy of different manufacturing configurations. Furthermore, LPBF lateral stiffeners were included in the workpiece design, thereby converting the final workpiece into a temporary assembly. The proposed methodology was applied in a case study for finishing thin-walled bent ducts and a comparison for surface quality between stiffened and non-stiffened ducts using the proposed methodology was conducted. A significant roughness and cutting force reduction (≈50%) were obtained for the stiffened duct.

1. Introduction

Additive manufacturing has resulted in the creation of a new segment in the manufacturing of complex-shaped metallic parts [1]. These processes have been studied for industrial applications in medium and small batch lots [2,3]. Certain aspects, such as the smooth integration between the 3D model and the manufacturer, excellent scalability, low design limitations with internal shapes, and lattice structures, render additive manufacturing a better option than other manufacturing techniques [4,5]. However, although in the context of Industry 4.0, additive manufacturing plays a key role, certain concerns regarding its application in large batch manufacturing exist [6]. Consequently, concepts such as group technology and production cells are essential to overcome this issue [7]. Additive manufacturing processes are of particular interest in the segment of thin-walled, hollow, and slender parts; nevertheless, post-processing, that is, machining, is necessary to guarantee the dimensional and surface quality of functional parts. Currently, combining additive and subtractive processes into a hybrid manufacturing method [8,9] has enabled the manufacture of functional parts for aeronautical engine parts, turbines, biomedical implants, and many other applications.

Recently, several studies have been conducted on the machining of LPBF-printed parts. Many of these studies have focused on analysing the surface quality, machinability, and microstructural characteristics of the material [10,11]. However, the surface quality of the as-printed LPBF components is not sufficient for functional applications, and post-processing by milling or a similar process is often needed [12]. Further, support fixtures are essential to ensure the stability of the milling process, affecting the surface and deflection of the workpiece [13]. However, milling complex LPBF parts is a challenge because of the necessity of support for manufacturing, affecting the stiffness of the part and resulting in vibrational problems that amplify the cutting instability, particularly for flexible structures. Consequently, certain industrial solutions have been provided for specific geometries through the use of special supportive workholding during finish machining [14]. Most recent studies have been based on machining prismatic or cylindrical workpieces with sufficient stiffness. Few studies focusing on the machining of near-net-shape parts for functional applications have been conducted [15], wherein thin walls and complex and slender shapes represent a machining challenge owing to the low stiffness of these components and the difficulties of implementing conventional fixture supports. The use of base-plate sacrificial supports for clamping and positioning AM workpieces to ensure fixation during the machining process has also been evaluated [16]; however, its optimisation is complex and not well known. Therefore, developing robust hybrid manufacturing methodologies [17] that include aspects related to the LPBF manufacturing process, machining parameters, part design, and microstructural characteristics of the material is essential.

The flexibility of the LPBF process is dependent on both the several complex shapes that can be manufactured and the improvement of the mechanical properties of the workpiece. This is because of the possibility of changing the distribution of the crystalline orientation in the material through the configuration of the laser power, laser speed, layer thickness, hatching space, and laser rotation strategy [18]. In this regard, Karimi et al. [19] established relationships between volumetric energy density, hardness level, and porosity, and Liu et al. [20] reported the interaction between LPBF parameters and anisotropy in mechanical properties through variations in the Taylor factor for different sample orientations. The different combinations of LPBF parameters allow different values of volumetric energy density and different solidification modes to be obtained, which translates into the control of the size and orientation of the grains and modification of the crystalline texture. Considering this, Lei et al. [21] analysed the effect of hatching space and laser speed on grain refinement, roughness, and microhardness, and concluded that volumetric energy density played a major role in these variables. Further, Yi et al. [22] explored the effect of linear energy density on yield strength. Components manufactured via LPBF are considered to be textured, rendering them anisotropic. Many authors consider that the primary cause of the anisotropy in mechanical properties is related to the development of ultrafine columnar grains that grow epitaxially along the building direction and preferred crystalline orientations [23–26]. The anisotropy in the Young's modulus of LPBF printed components indicates that the material exhibits much higher stiffness values for specific directions and shallow values in certain directions, which has been widely reported in the literature for the evaluation of as-printed LPBF [27] and heat-treated samples [28], and their interaction with the cutting process [29,30]. An essential factor in increasing the stiffness of a component from the design (CAD) and LPBF printing stages is the orientation of the printed parts. In addition, the mechanical properties of LPBF components can change even at the same energy density [31].

The high thermal gradient, fast cooling rates, and development of columnar grains in the LPBF process are the leading causes of crystalline gradients, residual stresses, and geometric distortions. In certain cases, the residual stresses and distortions can be minimised by optimising the manufacturing parameters or using fixture supports [32] Further, real-time monitoring can reduce the cost of non-quality, specifically in the case of premature failures. Certain works relate techniques that process monitoring through image analysis and detect anomalies to take action [33–35]. However, in certain cases, achieving the required mechanical properties is not possible using the LPBF process. This limitation can be overcome through the use of appropriate heat treatments to homogenise and increase the mechanical properties. Additive manufacturing processes cannot produce finished parts with narrow tolerances and optimal surface quality, even with optimised parameters. Therefore, post-processing using machining is often required.

Thus, this study proposes a methodology for increasing the stiffness of the components by increasing the Young's modulus and using temporary lateral stiffeners, which allows the printed components to behave as a temporary assembly, thereby decreasing the cutting forces and roughness levels. The methodology is based on an iterative design process, wherein the harmonic response of the component is analysed, considering the initial boundary deformation values, by testing different configurations and geometries for the lateral supports and evaluating the response of each configuration on the maximum amplitude of the displacement in the area of application of the cutting force. The methodology was evaluated through its application to a case study wherein temporary lateral stiffeners were introduced to increase the stiffness of Inconel 718 LPBF-angled ducts to improve the surface quality of the peripheral milling in the extreme zone of the ducts. The results for the first design iteration showed a significant improvement in the surface quality relative to the duct without stiffening.

In this paper, a methodology to improve the stiffness of near-net shape AM components has been proposed. Section 2 presents the five phases of the methodology. A case study is presented in the following sections to validate the proposed method. Section 3 presents a preliminary analysis of the machining features. In section 4, SEM and Electron backscattering scanning diffraction (EBSD) analyses are performed on the samples to obtain the texture, crystalline orientation distribution function (ODF), Hill stiffness tensor, and spatial distribution of Young's modulus to improve it. In Section 5, the duct stiffness is improved by implementing temporary lateral stiffeners with different configurations. Finally, multi-objective optimisation was performed to obtain the geometry of the stiffener. Section 6 presents the manufacturing phase and verification of the surface quality, and Section 7 presents the analysis of the current stiffening configuration performance.

2. Methodology

In this study, a methodology was proposed to improve the manufacturing process of low-stiffness LPBF parts using an iterative design process based on deformation boundary conditions. An initial configuration was proposed for the positioning of the components, which in turn were joined together by lateral stiffeners to achieve the required surface and dimensional quality. The methodology is divided into five phases: i) preliminary machining analysis, ii) enhancement of Young's modulus, iii) stiffness enhancement with lateral stiffeners, iv) manufacturing and verification, and v) analysis and improvement of the current stiffening configuration. Fig. 1 shows the general flow chart of the proposed methodology, and Fig. 2 shows the detailed steps within each stage and the specific interactions between stages.

In the preliminary machining analysis, an initial evaluation of cutting conditions, cutting forces, machining operations, tool geometry, and excitation frequencies was performed to detect whether the initial machining conditions required the use of conventional support systems or if the lateral stiffener method was a feasible option. If the cutting force levels are manageable, and the excitation frequencies are significantly lower than the natural frequency and chatter frequency, it is recommended to proceed to the second stage, that is, enhancement of Young's modulus

In the second stage, anisotropy is exploited to enhance the Young's modulus and improve the stiffness of the component owing to the anisotropic nature of the materials obtained through the LPBF process. For this purpose, it is recommended that it be started with a couple of parameter settings to obtain the stiffness tensor and Young's modulus distribution. On obtaining the Young's modulus, it is possible to compare the LPBF parameters and strategies that maximise Young's modulus with respect to the workpiece geometry and load state. Consequently, if the Young's modulus increases or anisotropy decreases, it is recommended to advance to the third stage, that is, stiffness enhancement with lateral stiffeners.

The third stage assesses whether the improvement in Young's modulus (second stage) is sufficient to achieve minimum stiffness. The evaluation begins by establishing a boundary deformation (δ_b) for the first iteration. If the workpiece stiffness is sufficient (the deformation caused by the cutting forces is lower than δ_b), it is possible to manufacture the part. However, if the stiffness is insufficient, but the sum of two or more stiffnesses of the workpiece surpasses the minimum stiffness, the lateral stiffeners may be an option. The unknown shape, size, and location of the temporary lateral stiffeners are necessary to design these elements. Once the stiffness enhancement reaches the objective, the manufacturing and verification stages can occur.

In the manufacturing and verification stages, the workpiece is fabricated according to the stiffening configuration that provides the best balance between the stiffener volume and deformation level. It is recommended that dimensional control of the LPBF component manufactured be exercised using lateral stiffeners to adjust the CAM program before the machining operations. Once the machining process finishes and the quality level is sufficient, the design can be considered appropriate. However, if the surface and dimensional quality are not achieved, it is recommended to decrease the value of boundary deformation(δ_b) and proceed to a new iteration in the design of the stiffening elements or increase the Young's modulus. In addition, conventional or special fixture support is recommended if the desired workpiece quality is not reached after certain iterations.

3. Preliminary machining analysis

The quantification of the cutting forces for various machining conditions is critical for a preliminary analysis. Thus, two samples of Inconel 718 LPBF were manufactured using a 67° laser scanning strategy. The samples have two zones, each with different layer thicknesses. The lower zone was manufactured with a $30\mu m$ layer while the upper zone with a $60\mu m$ layer. (See Table 1). The lower $30\mu m$ zone is hereafter referred to as lt30, and the upper $60\mu m$ zone as lt60. The purpose of these samples was to perform peripheral milling operations with radial cutting depths in the range of 0.1 to 0.5 mm at different feed rates. The milling operations were performed on the XZ plane of the specimens and the feed rate in the X-axis direction. The LPBF parameters used in manufacturing the samples, machining parameters, and tool geometry are listed in Table 1.

The layer thickness values used in the research were considered as boundary limits (considering the other selected LPBF parameters, see Table 1), considering the structural and quality issues needed in AM workpieces. Layers of 60 μm are often used to minimise
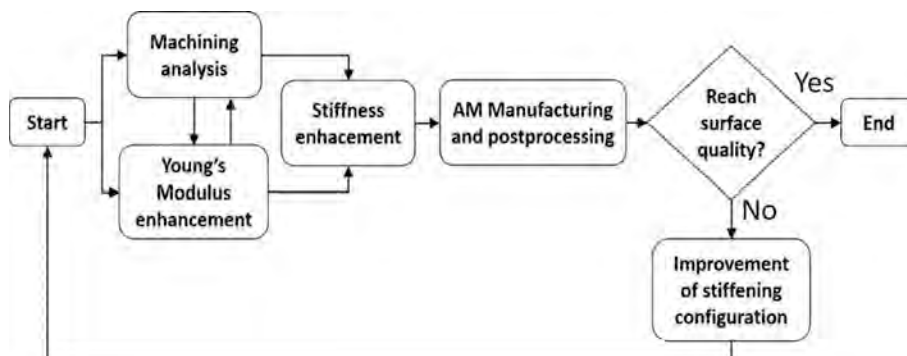

Fig. 1. Simplified LPBF functional part stiffening methodology scheme.
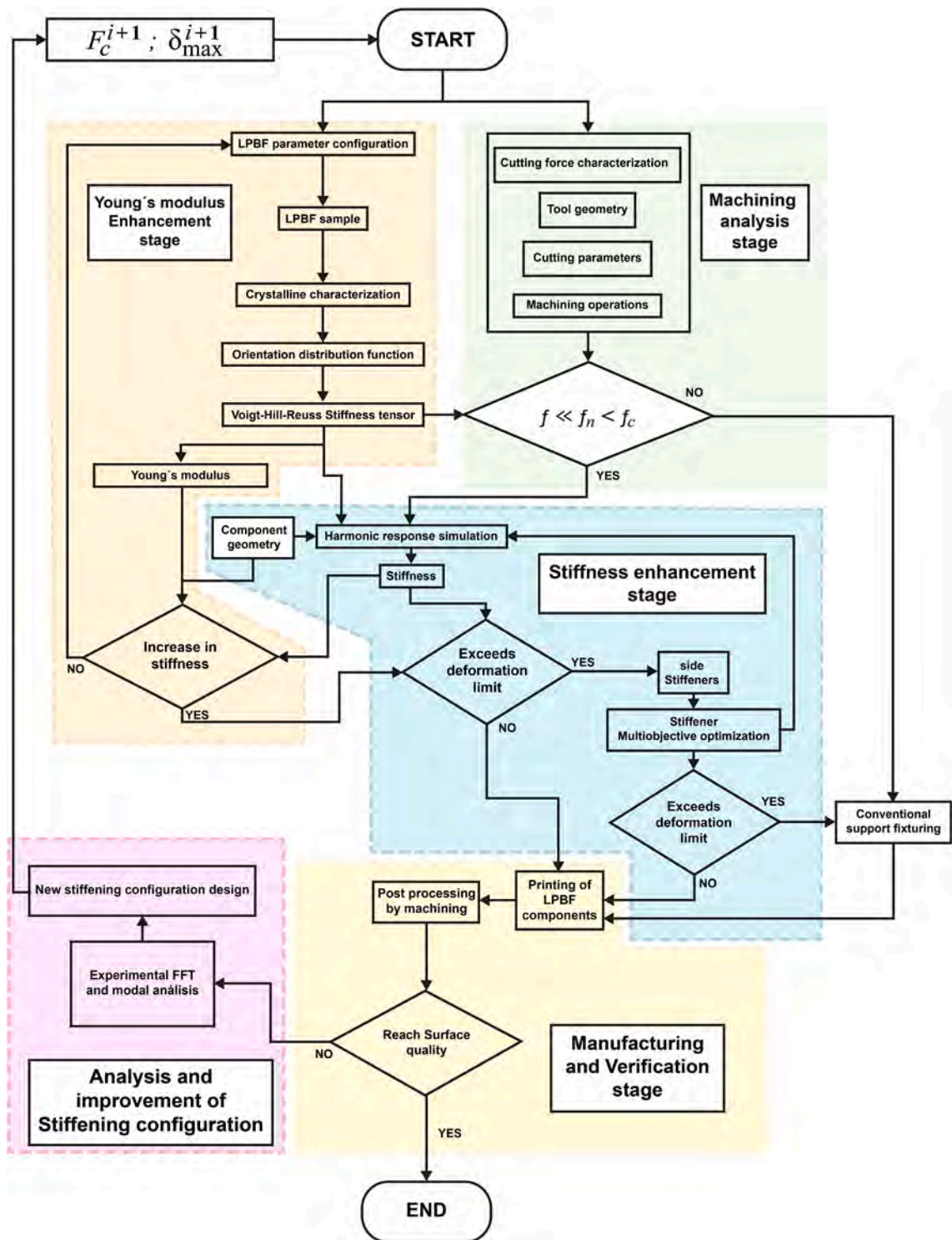
Fig. 2. Detailed Iterative LPBF stiffness enhancement component methodology flow scheme.

the processing time, while those of 30 μm are used when precision is required. However, layer thicknesses smaller than 30 μm are inconsistent with the feed powder size, and those greater than 60 μm on Inconel 718 are not recommended owing to the production of excessive internal porosity. In both cases (lt30 and lt60), the energy density was within the operating limits, avoiding the lack of fusion or balling effect.

Table 1

LPBF parameters, Cutting parameters, tool geometry, and LPBF sample geometry.

LPBF parameters		
	Zone 1 (lt30)	Zone 2 (lt60)
Power (W)	200	200
Speed (mm/s)	1000	1000
Hatch spacing (mm)	0.09	0.09
Layer thickness (μm)	30	60
Laser beam spot size (μm)	70	70

Cutting parameters and tool geometry	
Cutting speed V_c (m/min)	60
Axial depth a_p (mm)	5
Tool diameter (mm)	10
Helix angle β (°)	30
Flutes (z)	4

The nature of the LPBF process causes melting and solidification to occur almost simultaneously in each track and layer, and the laser heat-affected volume is in low proportion with respect to the overall workpiece volume, which reduces the possibility of significant geometric distortions due to residual stress. Consequently, a laser rotation strategy of 67° per layer was used, which is considered helpful in reducing the residual stress [36,37].

The LPBF samples and workpiece were manufactured using a Renishaw AM-400 machine and machining operations were performed in an Ibarmia ZV-25/U600 machining centre. Further, the cutting forces were measured using a dynamometer (Kistler 9225B) and an OROS data acquisition system.

The mean cutting forces corresponding to the parameters mentioned in Table 1 with feed rates f_z of 0.03, 0.04 and 0.05 mm/min and radial cutting depths a_e of 0.1, 0.3, and 0.5 mm, respectively, are listed in Table 2.

Another relevant aspect of this section is to define whether the excitation frequency due to the tooth passing frequency f is significantly lower than the natural frequency f_n of the workpiece and the chatter frequency f_c. This aspect can be evaluated by analysing the directional dynamic milling coefficient α_{yy}, which can be calculated using (1) [38].

$$\alpha_{yy} = \frac{1}{2}[-cos2\theta - 2K_r\theta - K_r sin2\theta]_{\phi_{st}}^{\phi_{ex}} \tag{1}$$

where θ is the engagement angle, K_r is the radial force coefficient, and ϕ_{ex} and ϕ_{st} are the exit angle and start angle, respectively.

Considering that the axial depth limit a_{lim} is always a positive value, it is suggested that the chatter frequency will be higher or lower than the natural frequency depending on the sign of the directional milling coefficient α_{yy} (see Equation (2)).

$$a_{lim} = \frac{1}{\frac{\Omega}{2\pi}\alpha_{yy}K_t Re[G_y(if_c).]} \tag{2}$$

where Ω is the spindle speed, K_t is the tangential force coefficient, and $Re[G_y(if_c).]$ is the real component of the transfer function of the workpiece in the Y-direction.

Further, several hammer tests were developed in the X and Y directions to obtain the experimental modal parameters (damping ratios and natural frequencies) (see Fig. 3a).

The transfer function of the workpiece in the Y-direction G_y, indicates the relationship between the natural frequency, chatter frequency, and modal parameters, and is expressed as Eq. (3).

$$G_y(if_c) = \frac{\frac{f_{ny}^2}{k_y}}{f_{ny}^2 - f_c^2 + 2\xi_y f_{ny} f_c i} \tag{3}$$

where k_y, ξ_y and f_{ny} are the stiffness, damping ratio, and undamped natural frequency, respectively, in the Y direction. Therefore, it

Table 2

Measured cutting forces by peripheral milling.

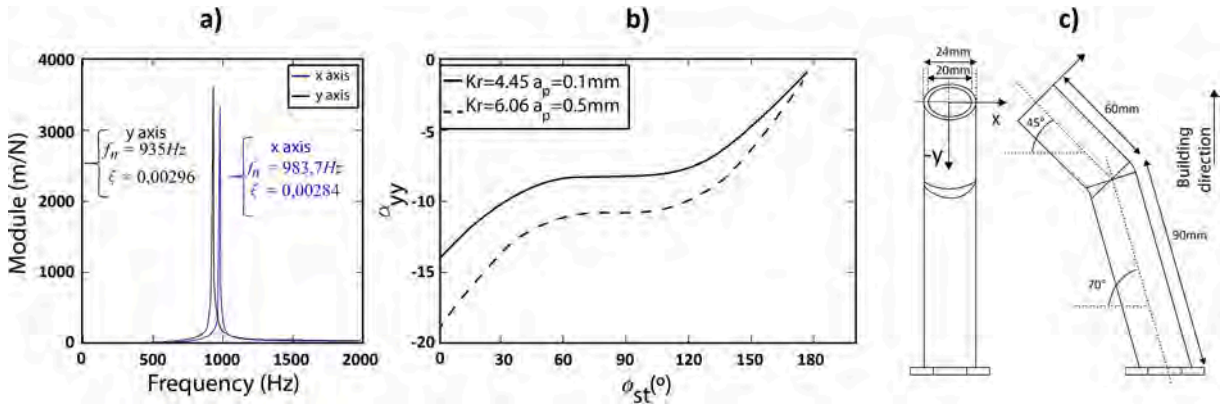| Layer thickness	$a_e(mm)$	$\overline{F_t}(N)$			$\overline{F_r}(N)$			$\overline{F_a}(N)$		
		$f_z(0.03)$	$f_z(0.04)$	$f_z(0.05)$	$f_z(0.03)$	$f_z(0.04)$	$f_z(0.05)$	$f_z(0.03)$	$f_z(0.04)$	$f_z(0.05)$
Lt30	0.1	12.2	16.0	19.4	19.4	27.5	34.4	3.7	6.2	7.0
	0.3	30.6	40.2	44.4	63.4	74.1	80.3	9.6	12.5	14.4
	0.5	49.3	57.3	73.1	102.1	111.6	118.2	14.7	19.1	21.8
Lt60	0.1	13.6	17.5	19.2	23.5	28.3	33.6	5.0	5.71	6.5
	0.3	27.7	32.7	44.6	62.7	70.2	74.8	7.5	10.0	27.9
	0.5	47.8	57.2	68.8	86.1	97.6	107.7	15.0	18.8	22.36

Fig. 3. Preliminary analysis: a) Hammer test results; b) directional dynamic milling coefficient α_{yy}; c) angled duct geometry.

can be defined that the chatter frequency f_c will be higher than the natural frequency f_n when coefficient α_{yy} has a negative sign. This is the case for down-milling. Fig. 3b shows α_{yy} related to the start angle ϕ_{st} when down-milling for $K_r = 4.45$ and 6.06, based on the cutting forces and axial depths in Table 2. The duct geometry is shown in Fig. 3c.

Considering that the excitation frequency f is 127 Hz (where $f = \frac{z*\Omega}{60}$, and z is the number of flutes in the tool), the natural frequencies are $f_{ny} = 935$ Hz, and $f_{nx} = 983.7$ Hz, and that the chatter frequency f_c is higher than the natural frequency (considering that α_{yy} has a negative sign, see Fig. 3b); therefore, $f << f_n < f_c$. Consequently, it is possible to establish that the excitation frequency is significantly lower than the resonance and chatter frequencies, and that the harmonics of the excitation frequency do not match the resonance frequency. The fulfilment of this condition allows the establishment of the geometrical characteristics of the workpiece and the improvement of the stiffness through the increase of the Young's modulus and the use of lateral stiffeners (following sections) would decrease the possibility of exciting resonance or chatter frequencies.

4. Young's modulus enhancement

Elastic anisotropy is an extended characteristic of LPBF components. This is mainly caused by the formation of columnar grains closely aligned in the building direction (BD) owing to the fast solidification of the melt pool tracks. Fig. 4 shows the SEM scans of the lt30 and lt60 samples and a comparison of the microstructures. The columnar dendritic grains in the lt30 sample are aligned with the
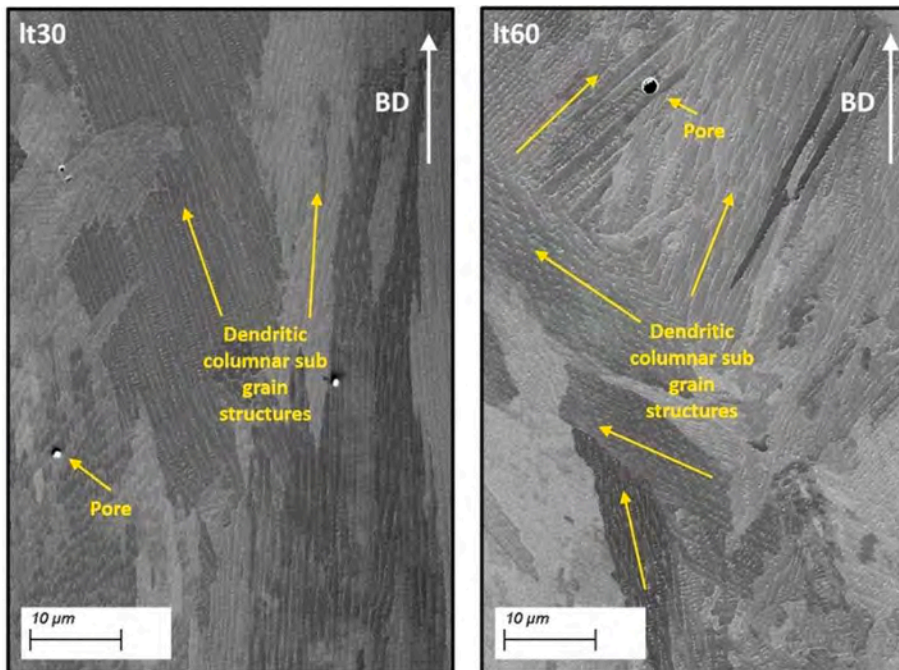

Fig. 4. SEM scans in lt30 and lt60 samples.

building direction. In contrast, the columnar grains in the lt60 sample present a broader range of orientations and a lower density of grains aligned in the building direction, which is related to the lower elastic anisotropy of the lt30 sample. Moreover, the lower volumetric energy density (VED) of the lt60 sample is the leading cause of stray grain development in this sample.

Additive manufacturing of metallic components is typically associated with anisotropy. Anisotropic mechanical properties counteract the application-specific advantages offered by the LPBF process. Initial investigations were conducted to evaluate the directional elastic modulus with varying layer thickness during the LPBF process. Based on these observations, the part was designed for the final milling operation.

Elastic anisotropy is often considered a drawback for LPBF manufacturing, and currently research has been focused on ensuring its reduction [39]. However, careful tailoring of the elastic anisotropy must be exploited during the design of additive manufacturing. If a specific direction of higher mechanical properties (yield strength, elastic modulus, etc.) of an LPBF component coincides with the longitudinal direction of the fabricated parts (critical stress direction), it may lower the milling force-induced deformation and vibration signatures. A primary advantage of the LPBF process is its flexibility in modifying the mechanical properties (Young's modulus) of the manufactured components according to the laser scanning strategy and manufacturing parameters. Further, obtaining sufficient stiffness in the LPBF workpiece is a significant aspect when avoiding poor surface quality due to excessive vibration, considering the significant effect of Young's modulus on stiffness.

The geometry of the angled ducts facilitates the easy optimisation of the Young's modulus without affecting other design considerations because these components are usually associated with tensile and compressive stresses[40] (by longitudinal loads or bending) in the longitudinal direction of the ducts (where Young's modulus has been optimised). However, for intricate shapes, the optimisation of Young's modulus by managing the anisotropic aspects must be carefully investigated.

The elastic stiffness matrix C_{ijkl} expressed as Eq. (4) relates the stress and strain tensors, based on which the elastic mechanical properties, including Young's modulus, are derived.

$$\sigma_{ij} = C_{ijkl}\varepsilon_{kl} \tag{4}$$

One approach to obtaining the stiffness matrix C_{ijkl} in polycrystalline materials as LPBF workpieces is using the Hill tensor $\langle T \rangle^{Hill}$ (Eq. (5)), which corresponds to the average of the Voigt $\langle T \rangle^{Voigt}$ and Reuss $\langle T \rangle^{Reuss}$ tensors (Eqs. (6) and (7)). The Hill tensor has been extensively used in the literature and has proven to be quite effective in obtaining the stiffness matrix from the crystal orientation density function (ODF).

The Voigt average specimen effective tensor $\langle T \rangle^{Voigt}$ is defined by the volume average of the individual tensors $T(g_m^c)$ with crystal orientation g_m^c and volume fraction V_m assuming that the strain field is constant. In contrast, the Reuss average effective tensor $\langle T \rangle^{Reuss}$ is defined by assuming that the applied tensor field is constant, which implies that the stress field is considered constant.

$$\langle T \rangle^{Hill} = \frac{1}{2}\left(\langle T \rangle^{Voigt} + \langle T \rangle^{Reuss}\right) = C_{ijkl} \tag{5}$$

$$\langle T \rangle^{Voigt} = \sum_{m=1}^{M} V_m T(g_m^c) \tag{6}$$
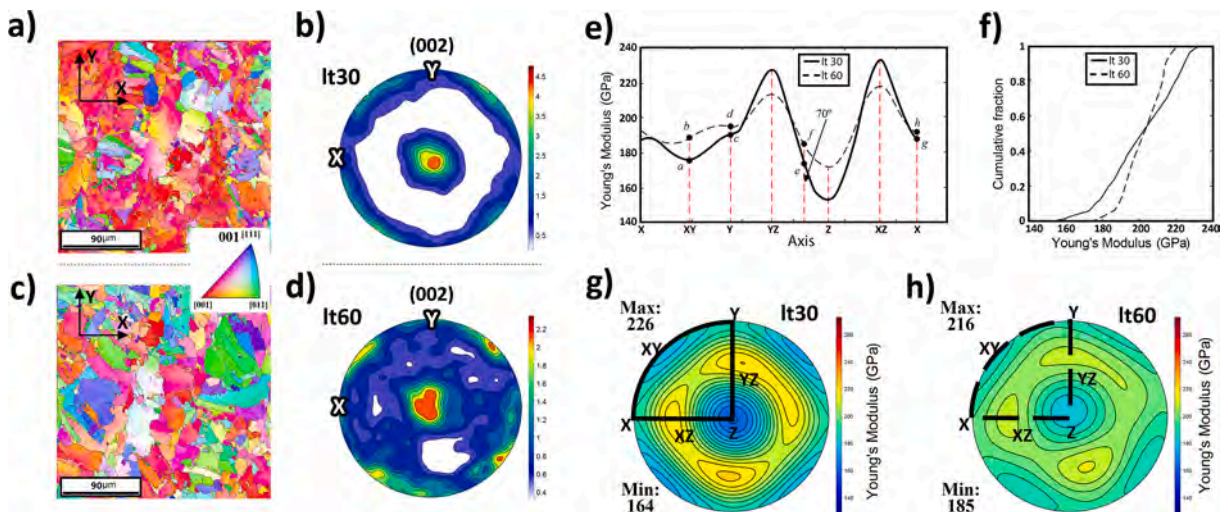

Fig. 5. a), c). Inverse pole figures for lt30 and lt60 samples; b), d). Pole figures of crystallographic texture in lt30 and lt60 samples; e), f), g), h). Spatial Young's modulus distribution in lt30 and lt60 samples.

Table 3
Voigt-Reuss-Hill Elastic stiffness tensor for lt30 and lt60 samples.

Lt30							Lt60						
$C_{ij}(GPa)$	1	2	3	4	5	6	$C_{ij}(GPa)$	1	2	3	4	5	6
1	285.36						1	283.41					
2	127.00	283.28					2	129.05	285.05				
3	141.34	143.42	268.94				3	141.24	139.59	272.87			
4	−0.63	−2.37	3	89.06			4	1.14	2.09	−3.23	84.08		
5	0.13	−1.33	1.2	−0.99	86.		5	2.4	0.58	−2.98	−0.5	86.08	
6	1.21	−0.41	−0.8	−1.37	−0.71	70.43	6	−1.61	2.10	−0.49	0.65	1.27	72.49

$$\langle T \rangle^{Reuss} = \left[\sum_{m=1}^{M} V_m T^{-1} \left(g_m^c \right) \right]^{-1} \tag{7}$$

In Voigt notation Young's modulus $E(x)$ is expressed as Eq. (8)

$$E(x) = \left(S_{ijkl} x_i x_j x_k x_l \right)^{-1} \tag{8}$$

where x is the direction of Young's modulus, and S_{ijkl} is the elastic compliance tensor, which is expressed as Eq. (9):

$$S_{ijkl} = \frac{1}{C_{ijkl}} \tag{9}$$

Samples lt30 and lt60 were analysed via EBSD to obtain the orientation density function (ODF) and elastic stiffness matrix C_{ijkl}. Fig. 5a and 5c show the inverse pole figures (IPF) obtained from EBSD scans of lt30 and lt60 samples in the YX plane. In addition, Fig. 5b and 5d show the texture pole figures for the lt30 and lt60 samples, respectively. Both samples showed a ring-like $\langle 0\,0\,1 \rangle$ texture. Further, the lt30 sample was significantly intense, with a maximum probability density of 5. Moreover, in both samples, the ring-like effect in the texture was caused by the laser rotation strategy. Pole figures and IPF figures were obtained using MTEX from lt30 and lt60 ODF data.

Laser scanning strategies are associated with the crystalline texture patterns observed in pole figures [29]. Subsequently, the ODF represented in the texture pole figures can be related to the Young's modulus spatial distribution patterns [41], rendering the proposed methodology repeatable.

The spatial distribution of Young's modulus for both samples is shown in Fig. 5e, 5f, 5 g, and 5 h, where a higher degree of anisotropy is evident in sample lt30. In a similar manner, it is observed that in both samples, the Young's modulus is minimum in the Z direction (150 and 175 GPa) and maximum in the XZ (230 and 220 GPa) and YZ (225 and 212 GPa) directions. Considering that section A of the duct (Fig. 3b) has an orientation of 70° in the YZ plane, it can be inferred from Fig. 5e that the lt60 sample has a higher Young's modulus (190 GPa) compared to the lt30 sample (175 GPa) for the orientation previously mentioned.

Table 3 presents the Voigt-Reuss-Hill elastic stiffness tensor for the lt30 and lt60 samples obtained from the ODF data. The lower elastic anisotropy of the lt60 sample and its higher Young's modulus, owing to its geometry, render it a better choice for the manufacture of the angled duct; therefore, a layer thickness of 60 μm was used to manufacture the case study workpiece and evaluate the stiffness-based methodology proposed in this work.

5. Stiffness enhancement with lateral stiffeners

This stage aims to propose decision criteria to evaluate the initial stiffness of the part with the previously improved Young's modulus and determine whether the part has sufficient stiffness to proceed to the manufacturing stage (case 1). If the stiffness of the workpiece is insufficient, additional lateral stiffening is necessary (case 2). In contrast, if the additional lateral stiffness is insufficient, it is necessary to stiffen the part using specific or conventional support fixtures (case 3) and remove the printed part from the base plate to perform the machining operations.

The following decision criterion is proposed using Eqs. (10)–(12).

$$\begin{cases} if \ K_{wx\_b}^i < K_{wx}^i \ then \ case & (10) \\ if \ K_{wx\_b}^i > K_{wx}^i \ and \ K_{wx\_b}^i < nK_{wx}^i \ then \ case \ 2 & (11) \\ if \ K_{wx\_b}^i > nK_{wx}^i \ then \ case \ 3 & (12) \end{cases}$$

where $K_{wx\_b}^i$ is the boundary stiffness of the workpiece for iteration (i) in x direction, K_{wx} is the actual stiffness of the workpiece in x direction, n is the number of parts that fit on the base plate. and $K_{wx\_b}^i$ is obtained according to Eq. (13)

$$K_{wx\_b}^i = \frac{F_c^i}{\delta_{b\_x}^i} \tag{13}$$

Table 4
Parameters for iteration 1.

Parameters for $i = 1$	
$\delta_{b\_x,y,z}^1 (mm)$	0.1
Tooth passing freq (Hz)	127
$a_e (mm)$	0.1
$\overline{F_t}(N)$	19.4
$\overline{F_r}(N)$	34.4
$\overline{F_a}(N)$	7
S_1	6

where $\delta_{b\_x}^i$ is the boundary deformation and F_c^i is the resultant cutting force obtained from the tangential, radial, and axial force components, as defined in Eqs. (10–13), applicable for x, y, z in the workpiece reference frame.

Considering that the milling of flexible elements implies an increase in the cutting force related to the characterised forces (Table 2), it is recommended that the selected cutting forces F_t^i, F_r^i, F_a^i be adjusted by a coefficient, as expressed in (14).

$$F_t^i = \overline{F_t}S_i \quad F_r^i = \overline{F_r}S_i \quad F_a^i = \overline{F_a}S_i \tag{14}$$

where $\overline{F_t}, \overline{F_r}, \overline{F_a}$ are the average forces measured for the selected cutting conditions (from Table 2), and S_i is the selected safety factor for iteration i.

The parameters established for the iteration $i = 1$ in the case study are summarised in Table 4.

For the case study, the resulting cutting force F_c^1, and the boundary stiffness $K_{b\_min}^1$ were 240.6N and 2406N/mm, respectively. Based on this, the criteria defined in Eqs. (10–14) can be evaluated.

The analysis of the harmonic response was conducted in ANSYS® for a frequency ranging from 0 to 300 Hz, angle $\boldsymbol{\alpha}$ from 0° to 90°, and a damping ratio of 0.003, where $\boldsymbol{\alpha}$ represents the angular position of the tool relative to the workpiece, as shown in Fig. 6. Force-induced deformation and stiffness of the ducts were obtained across an $\boldsymbol{\alpha}$ range of 90°. Harmonic response simulations for the lt30 and lt60 samples are shown in Fig. 7a. Simulations were conducted using the elastic properties obtained using the Hill elastic stiffness tensors, as shown in Table 3.

Based on the results of the first simulation (Fig. 7a), it is worth noting that the lt60 sample has a greater stiffness (1560 N/mm) at 127 Hz (tooth passing frequency) than the lt30 sample; however, it does not exceed the boundary stiffness; therefore,

$$K_{w\_lt30}^1 < K_{w\_lt60}^1 < K_{w\_b}^1 \tag{15}$$

The evaluation of Eq. (15) implies that Case 1 is not fulfilled, and Case 2 must be assessed.

To evaluate whether case 2 was fulfilled, harmonic response simulations were developed under six configurations with different lateral stiffening positions. Fig. 6b shows the scheme of the evaluated configurations and the deformations δ_x^1 and δ_y^1 under the previously mentioned excitation conditions. Fig. 7b shows that configurations 4 and 6 satisfy the criteria of Case 2. In addition, to advance the investigation, configuration six was selected because it maximises productivity and fits in the base plate of the LPBF machine.

Because lateral stiffening is feasible, the next step is to define the location, geometry, and size of the temporary stiffeners. For this purpose, new harmonic simulations using different stiffener dimensions were performed with configuration 6. Two aspects were considered for the shape of the temporary stiffeners: first, vertical supports were not added, and second, the direction of maximum Young's modulus. Consequently, the stiffener angle relative to the base plate was fixed at 45°. Fig. 7c shows the maximum deformation for different values of width W and thickness t of the temporary lateral stiffeners for frequencies in the range of 0–2000 Hz. In a complementary manner, the Pareto front was obtained from a multi-objective optimisation, as shown in Fig. 7d.

The multi-objective optimisation was conducted between the duct deformation function and the stiffener volume function, determining the minimum stiffener volume to obtain the minimum duct force-induced deformation and waste of material, considering that the lateral stiffeners were temporary elements that must be removed after machining. The results obtained allowed the establishment of width ($W = 12mm$) and thickness ($t = 1mm$) values for iteration i = 1. Further, to realise multi-objective optimisation, a genetic algorithm function (MATLAB) was applied, considering a double vector population type, a population size of 100, the lower
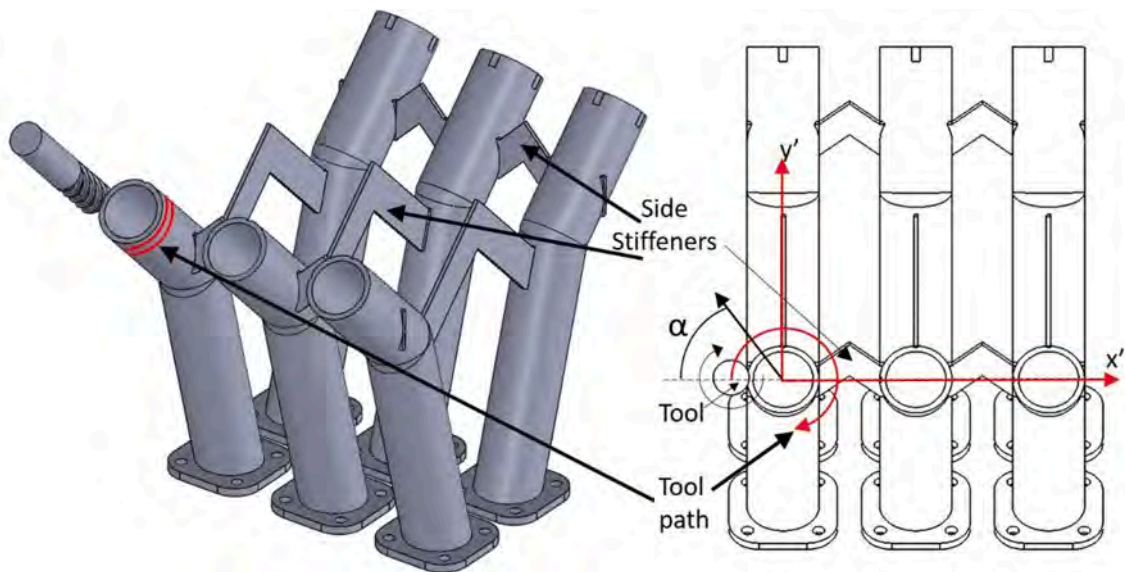

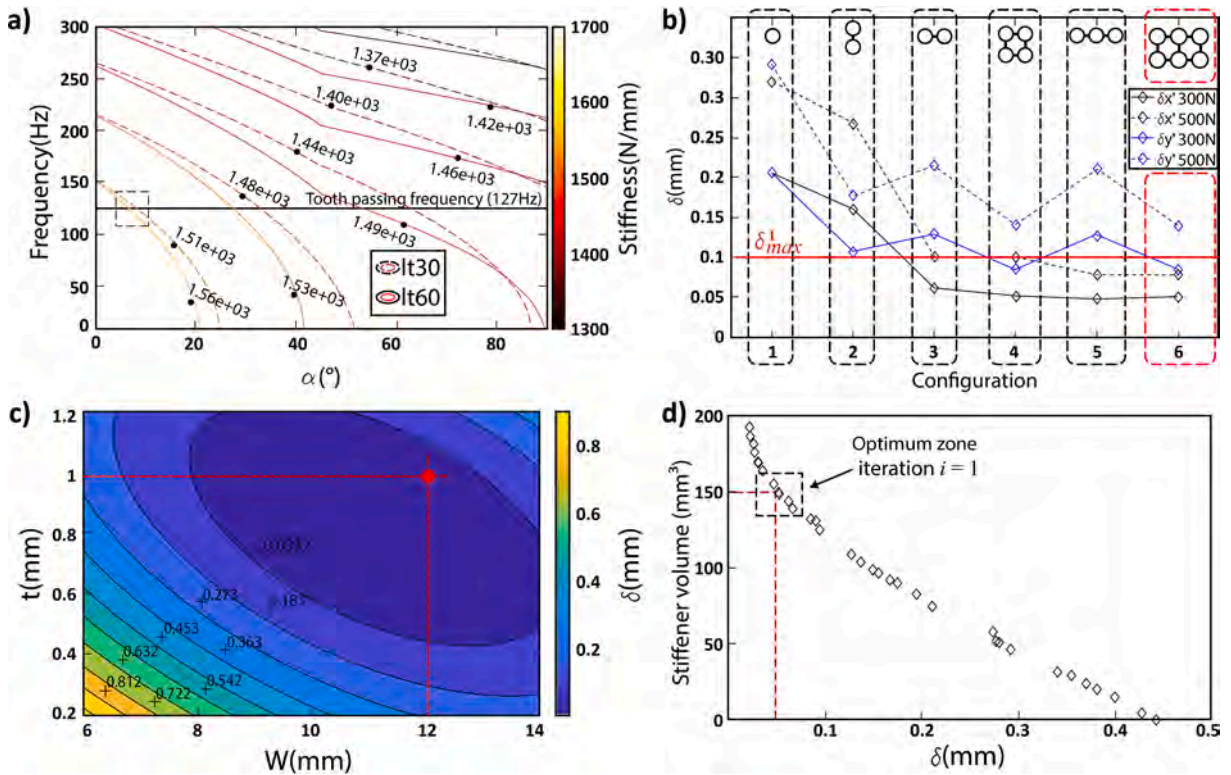**Fig. 6.** Workpiece geometry with lateral stiffeners.

Fig. 7. Stiffener design phase: a) Stiffness by α and frequency for lt30 and lt60 samples; b) elastic deformation by configuration; c) elastic deformation by t and W with configuration six; d) Pareto front for multiobjective optimisation.

and upper bounds according to volumetric restrictions, 100 generations, 100 stall generations, a function tolerance of 1e-4, and a constraint tolerance of 1e-3.

6. Manufacturing and verification

Once the simulation and design phases of the lateral stiffeners were completed, six laterally stiffened ducts with a layer thickness of 60 μm were fabricated according to Configuration 6. The stiffeners are located in a machining-free zone close to the duct extreme to increase stiffness, and an easily removable design was chosen (Fig. 8b). The steady-state stiffness was verified for Configuration 1 and 4; the experimental values were observed to be quite similar to the values simulated using ANSYS, as shown in Fig. 8c.

Before conducting any milling process, the geometric distortion of the manufactured part was verified using computed tomography. The analysis was conducted in a GE SEIFERT X-CUBE compact 195 KV with a minimum voxel size of 90 μm, and the data were evaluated using GOM Inspect 2019 software. Fig. 9 shows that the dimensional deviation in the area to be machined is in the order of 0.1 to 0.2 mm.
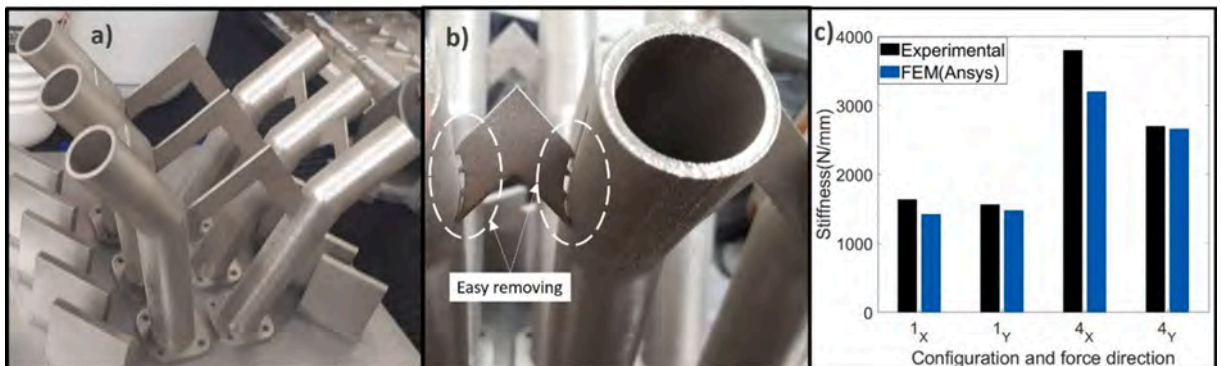

Fig. 8. LPBF Workpiece a) as printed; b). Lateral stiffener with easy removing; c). Measured vs. FEM stiffness.
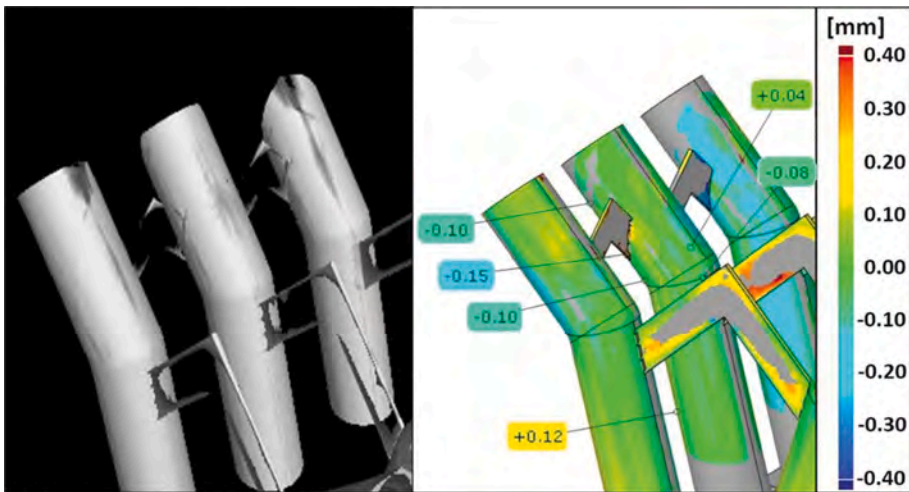
Fig. 9. Geometric distortion analysis: a) Computed tomography scan of LPBF workpiece; b) dimensional control or LPBF workpiece.
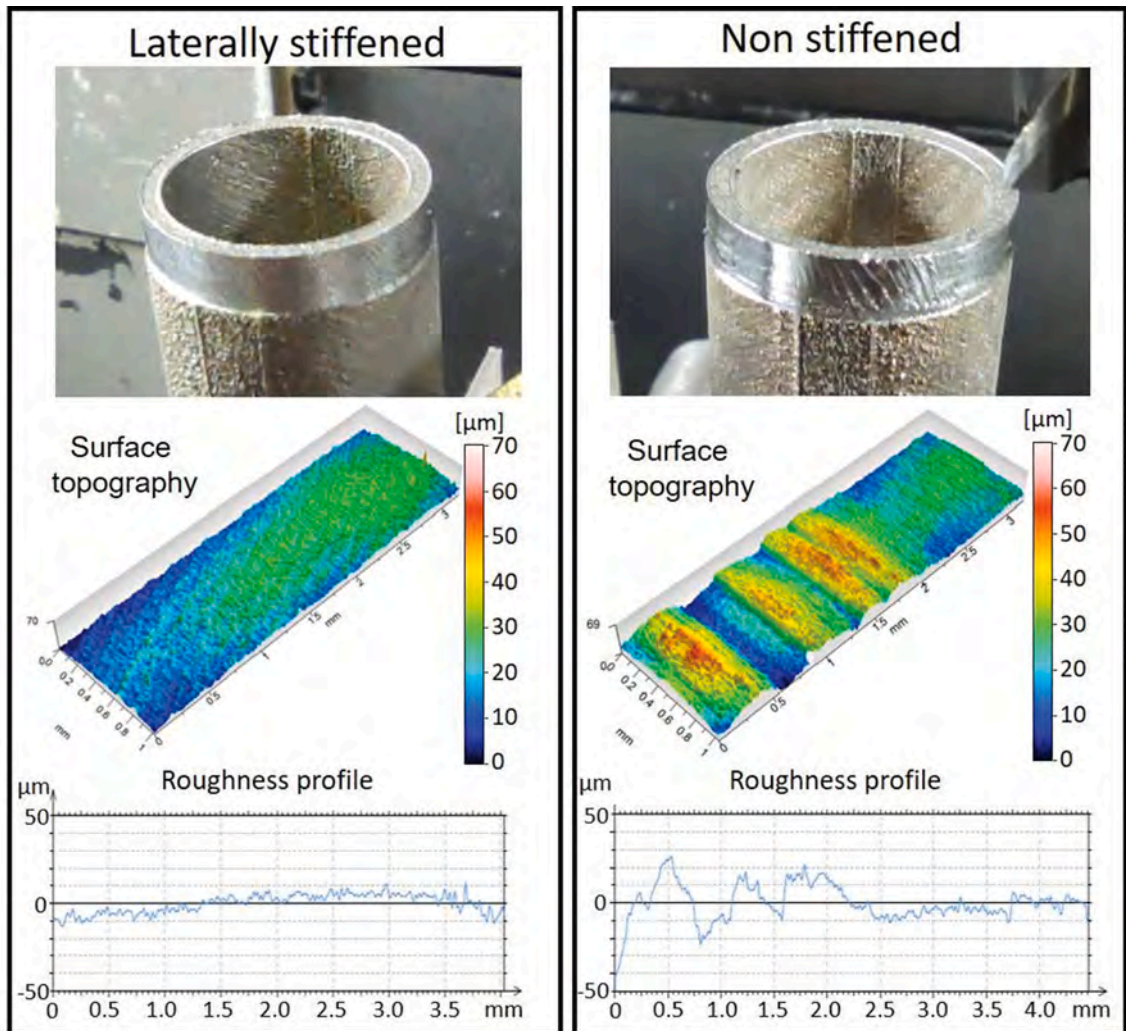

Fig. 10. Surface quality and roughness comparison between stiffened and unstiffened ducts after the milling process.

Once the level of geometric distortion was evaluated and the tool path was adjusted in the CAM program, peripheral milling was performed at the duct extreme for Configuration 4 (with lateral stiffeners) and Configuration 1 (without any lateral stiffeners). The cutting parameters were as follows: radial depth of cut $a_e = 0.1mm$, axial depth of cut $a_p = 5mm$, cutting speed $V_C = 60m/min$ feed rate per tooth $f_z = 0.05m/min$.

Fig. 10 compares the surface quality after peripheral milling of the stiffened duct (left) and unstiffened duct (right). Visually, the unstiffened duct exhibited inferior surface quality, with visible tool marks. The effect of stiffness of the set tool workpiece was also observed by analysing the surface topography and roughness profile. The stiffened duct presented a smoother and constant deviation along with the manufactured profile, with an apparent magnification of the deviation in the region manufactured by the tool's extreme. However, in the non-stiffened duct, the magnification due to the tool load cannot be identified because of the severe oscillations of the tool and the marks left. In addition, without the use of stiffeners, the roughness profile surpasses the target limits recommended for finishing

Fig. 11 shows the FFT frequency spectra of the force signal according to the angular position θ during the peripheral milling of the duct. In addition, a dephased of 45 °concerning the X'-axis (see Fig. 13) was used to ensure good engagement of the tool workpiece. In Fig. 11a (unstiffened duct), it can be observed that the force amplitude reached significant peaks of force amplitude for the tooth passing frequency and for the first mode of vibration (natural frequency), indicating that during the machining of the unstiffened duct, the resonance and chatter frequencies were excited. Further, in the case of the stiffened duct (Fig. 11b), the FFT analysis of the force signal exhibits lower amplitude levels for the tooth passing frequency; however, significant peaks were observed at angular positions of 90 °and 270 °. In these regions, through the modal analysis (CAE), a correlation with the sixth vibration mode (1418 Hz) was observed, indicating the direction to improve the design of the stiffeners in a subsequent iteration. This aspect is further discussed in Section 7.

The roughness Ra (Fig. 12a) and Rz (Fig. 12b) are shown as functions of θ for both stiffened and unstiffened ducts. It is evident that the roughness levels for the unstiffened duct across all θ ranges were almost double that of the stiffened duct. Furthermore, the stiffened duct roughness exhibits low fluctuations across the θ range, whereas for the unstiffened duct, the increase in Ra is significant between θ values of 90° (2 μm) and 270° (3.6 μm).

Fig. 12c shows the instantaneous cutting force as a function of θ during the machining of both ducts. In the case of the stiffened duct, it is observed that the resultant forces fluctuate between 10 and 20 N, whereas for the unstiffened duct, the forces fluctuate between 20 and 70 N, that is, five times more. Further, a sudden increase in the resultant force is observed when θ is equal to 50 °and 180 °for the unstiffened duct, which increased the instability of the process and magnified the roughness in the surrounding mechanised areas, as shown in Fig. 12a and 12b. In a similar manner, it is evident that the reduction of the resultant cutting force did not instantaneously improve the roughness, resulting in a delay in stabilisation. A more stable milling process is achieved using lateral stiffeners, with a significant decrease in roughness and cutting forces; therefore, stiffeners represent a valuable and economical alternative for controlling surface quality in LPBF parts that require finish machining operations. In addition, it is possible to infer that the current stiffener shapes, dimensions, and locations represent a good initial approximation for the complete design of the temporary assembly, which can be improved during subsequent stages of optimisation of the LPBF parameters and stiffener design.

7. Analysis and improvement of current stiffening configuration

The observed peaks in the cutting force at frequencies corresponding to the sixth mode of vibration (1418 Hz) for values of θ equal to 90 °and 270 °during the machining of the stiffened duct (see Fig. 11b) resulted in the performing of a new analysis of the stiffening design to improve the performance of the manufacturing processes. In Fig. 13, the x' axis is aligned with the direction of the main stiffener, and the Y' axis with the secondary stiffener. The vector field shows the resultant cutting force in the plane of the feed
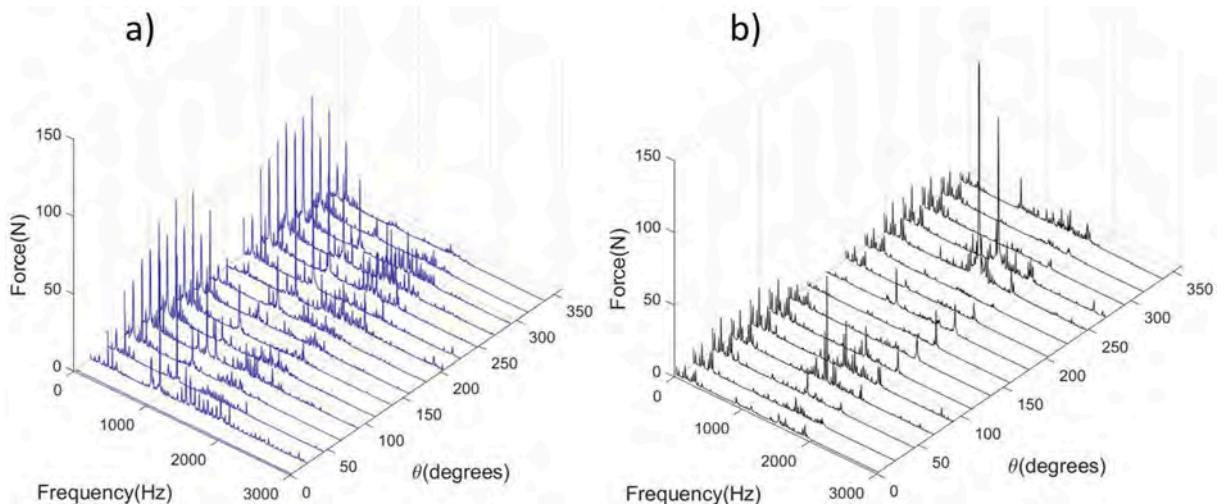

Fig. 11. FFT Cutting force-frequency spectra as a function of θ: a) Unstiffened duct, b) Stiffened duct.
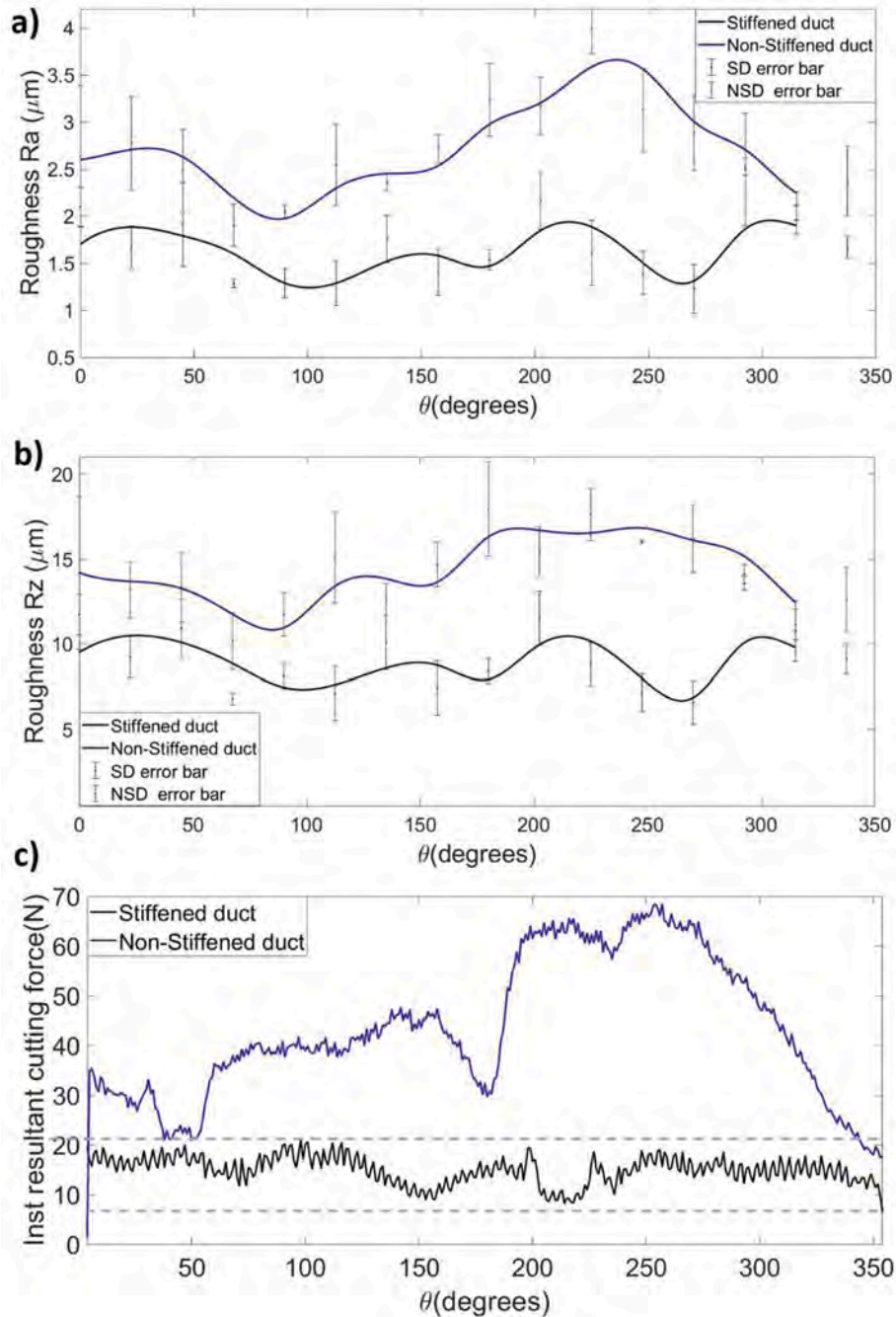
Fig. 12. Roughness and cutting force as a function of θ: a) Ra; b) Rz; c) Instantaneous resultant cutting force.

direction as a function of θ. Point A corresponds to the initial position of the tool, which advances clockwise. Further, the regions at the outer perimeter of the duct were marked by B, C, E, F, H, I, K, and L to represent the machined areas where the surface topography was evaluated.

From Fig. 13, it is evident that the resultant cutting force vectors at points D (θ = 90°) and J (θ = 270°) are oriented in the direction of the main stiffener (X' axis). In addition, it is evident that the sixth vibration mode direction was excited at the angular positions between D, E, K, and J (Fig. 14c). However, the resultant vector of the resultant cutting force near region G (Fig. 13) aligned with the secondary stiffener (Y' axis) and the direction of the third mode of vibration (see Fig. 14b). Consequently, it is possible to establish a relationship between the orientation of the resultant cutting force vector, the position of the stiffeners, and the maximum amplitudes of the cutting force as a function of the angle θ. Furthermore, when θ is equal to 180°, the cutting force peak reaches its highest amplitude for the third mode of vibration (1033 Hz), and the same is observed for θ values of 90° and 270° for the sixth mode of vibration (1418
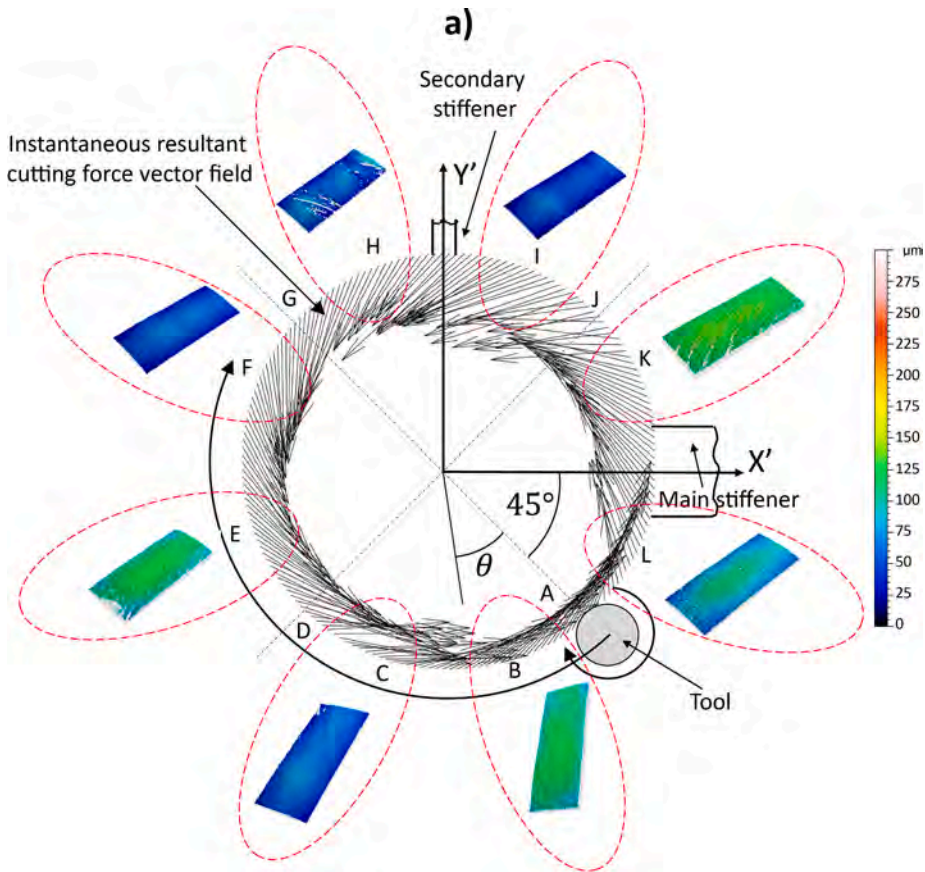
Fig. 13. Instantaneous resultant cutting force vector field and surface topography as a function of θ.
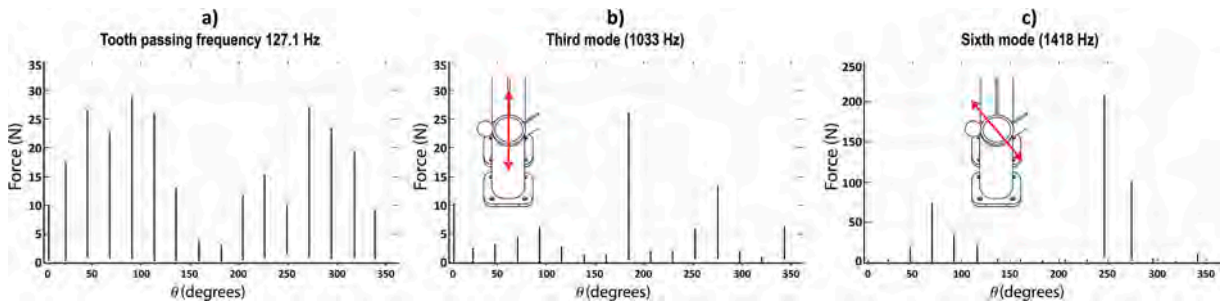

Fig. 14. a), b), c) Cutting force amplitude as a function of θ for tooth passing frequency, the third mode, and sixth mode in stiffened duct.

Hz).

Based on the above, it can be inferred that the largest cutting force amplitudes occur when the resultant cutting force vectors are aligned with the position of the stiffeners. In turn, the observed peak cutting force amplitude is proportional to the stiffener capacity, which is evident when comparing the low peak in Fig. 14b (when the resultant force vector is aligned with the secondary stiffener) with higher peaks in Fig. 14c (when the resultant force vector is aligned with the main stiffener). In addition, it is observed that the surface quality in the machined areas (see Fig. 13) at angles after the force peaks were lower than those observed before the force peaks. For example, the quality at C was better than that at E. This is also true when comparing F with H and I with K, implying that to improve the surface quality and decrease the variability of cutting force peaks, the stiffener design and its position must ensure sufficient duct stiffness homogeneity across all θ ranges, which should be considered in the configuration and design of the stiffeners for subsequent iterations.

Fig. 15 compares the current configuration of the stiffeners (IT 1) with the proposed configuration for the next iteration (IT 2). In the proposed configuration (IT 2), three aspects were considered based on the analysis. Primarily, there is a reduction in the distance
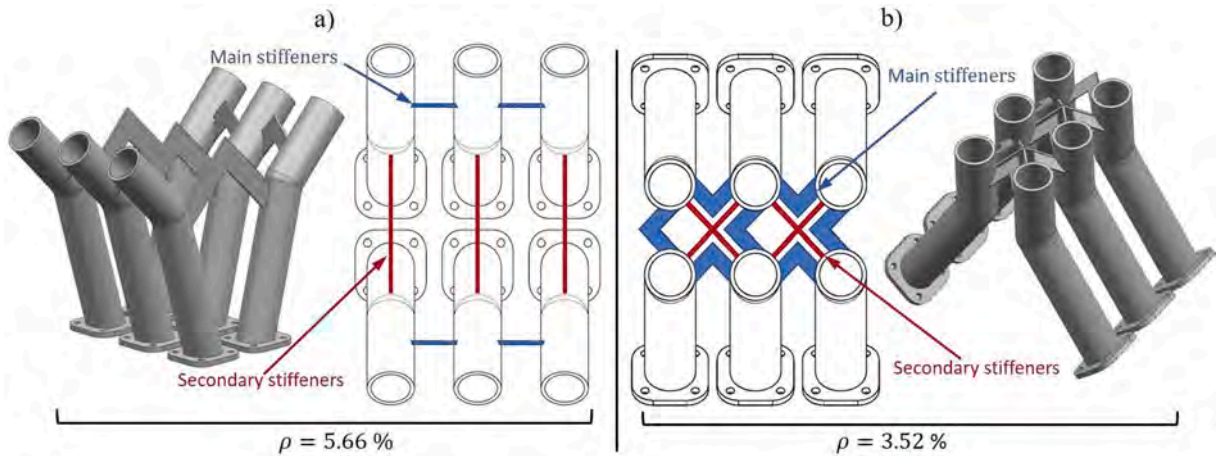
Fig. 15. a) Current stiffening configuration; b) the proposed stiffening configuration for a second iteration.

between the ducts to improve stiffness, which has been obtained on rotating ducts by $45°$ to the base plate, ensuring the vertical orientation of the duct extreme (Fig. 15b). Further, three stiffeners per duct have been proposed, consisting of two main stiffeners peripherally $90°$ to each other with $45°$ inclination to the duct extreme orientation. The inclination from the duct extreme ($45°$) provided maximum support to the duct perimeter. The third stiffener was oriented vertically between the two main stiffeners to counteract the chances of diagonal deformation. Finally, a lower stiffener volume fraction ρ (%) was proposed for IT 2 (3.52 %) than IT 1 (5.66 %), as shown in Eq. (16).

$$\rho(\%) = \frac{Stiffeners \quad volume(mm^3)}{Ducts \quad volume(mm^3)} \times 100 \tag{16}$$

8. Conclusions

A methodology for increasing the stiffness of components manufactured using LPBF was proposed in this study. The cutting forces of the two Inconel 718 samples were characterised using different machining parameters. In addition, the crystalline texture of both samples and their respective elastic tensors were obtained to quantify the effect of anisotropy on the Young's modulus. Subsequently, a case study was performed wherein the steps established in the methodology were applied for the first iteration of the design process of the lateral stiffeners, which resulted in a significant improvement in the surface quality compared to a non-stiffened part.

The main results are detailed below.

- The proposed methodology for increasing the stiffness of components manufactured by LPBF through the use of temporary lateral stiffeners can be a viable and low-cost alternative for finishing machining operations on this type of component. The machining operations can be performed with the parts attached to the base plate and without the need for additional support fixturing.
- The simulation of the harmonic response of the component by FEM represents a quick way to obtain an initial approximation of the effect of the cutting force on the vibration amplitude. The iterative nature of the proposed methodology implies that the deviation between the actual vibration values and the values obtained via simulation becomes increasingly smaller because the information of the surface quality, cutting forces, and vibration magnitude during the previous iteration allows the design and location of the lateral stiffeners to be improved in the following phases of design iteration and optimisation. Therefore, it is essential to develop specific methodologies for the design of lateral stiffeners based on component topology, geometry, and application.
- The similarity between the FEM and measured stiffness shows that the VOIGT-REUSS-HILL theory is an appropriate alternative to obtain the elasticity tensor and quantify the anisotropy in the mechanical properties. In the case evaluated, a 10% increase in Young's modulus was observed in the lt60 sample compared to the lt30 sample for the most extended area of the duct analysed. In addition, the lt60 sample exhibited a less dense 001 ring-like texture relative to the lt30 sample, which was reflected in a lower level of elastic anisotropy in lt60 sample compare to the lt30 sample.
- The significant difference in surface quality obtained in the first iteration allowed the establishment of temporary lateral stiffeners to be viable. The roughness profile showed an average maximum difference of 15 μm along the axial direction of the duct in the machined zone for the stiffened duct, whereas this difference increased to more than 90 μm in the unstiffened duct. In a similar manner, the cutting forces were almost five times higher in the unstiffened duct than in the stiffened duct.
- The analysis of the current stiffening configuration establishes that the stiffness of the ducts should be as homogeneous as possible along the duct perimeter. This implies that the stiffeners should cover the perimeter of the ducts as much as possible.

CRediT authorship contribution statement

José David Pérez: Conceptualization, Methodology, Writing – original draft, Writing – review & editing. **Felipe Marin:** Methodology, Validation. **Silvia Martínez:** Resources, Writing – review & editing. **Aitzol Lamikiz:** Supervision, Resources. **Gorka Urbikain:** Conceptualization, Methodology, Supervision, Writing – review & editing. **Luis Norberto López de Lacalle:** Methodology, Supervision.

Declaration of Competing Interest

The authors declare that they have no known competing financial interests or personal relationships that could have appeared to influence the work reported in this paper.

Acknowledgements

References

[1] C. Klahn, B. Leutenecker, M. Meboldt, Design strategies for the process of additive manufacturing, Procedia CIRP 36 (2015) 230–235, https://doi.org/10.1016/J.PROCIR.2015.01.082.

[2] S. Ford, M. Despeisse, Additive manufacturing and sustainability: an exploratory study of the advantages and challenges, J. Clean. Prod. 137 (2016) 1573–1587, https://doi.org/10.1016/J.JCLEPRO.2016.04.150.

[3] W. Gao, Y. Zhang, D. Ramanujan, K. Ramani, Y. Chen, C.B. Williams, C.C.L. Wang, Y.C. Shin, S. Zhang, P.D. Zavattieri, The status, challenges, and future of additive manufacturing in engineering, Comput. Des. 69 (2015) 65–89, https://doi.org/10.1016/J.CAD.2015.04.001.

[4] S.A.M. Tofail, E.P. Koumoulos, A. Bandyopadhyay, S. Bose, L. O'Donoghue, C. Charitidis, Additive manufacturing: scientific and technological challenges, market uptake and opportunities, Mater. Today. 21 (2018) 22–37, https://doi.org/10.1016/J.MATTOD.2017.07.001.

[5] M.K. Thompson, G. Moroni, T. Vaneker, G. Fadel, R.I. Campbell, I. Gibson, A. Bernard, J. Schulz, P. Graf, B. Ahuja, F. Martina, Design for additive manufacturing: trends, opportunities, considerations, and constraints, CIRP Ann. 65 (2016) 737–760, https://doi.org/10.1016/J.CIRP.2016.05.004.

[6] U.M. Dilberoglu, B. Gharehpapagh, U. Yaman, M. Dolen, The Role of Additive Manufacturing in the Era of Industry 4.0, Procedia Manuf. 11 (2017) 545–554, https://doi.org/10.1016/J.PROMFG.2017.07.148.

[7] C. Mosier, L. Taube, The facets of group technology and their impacts on implementation—a state-of-the-art survey, Omega 13 (5) (1985) 381–391, https://doi.org/10.1016/0305-0483(85)90066-0.

[8] J.M. Flynn, A. Shokrani, S.T. Newman, V. Dhokia, Hybrid additive and subtractive machine tools – Research and industrial developments, Int. J. Mach. Tools Manuf. 101 (2016) 79–101, https://doi.org/10.1016/J.IJMACHTOOLS.2015.11.007.

[9] G. Manogharan, Hybrid Manufacturing: Analysis of Integrating Additive and Subtractive Methods., 2014. https://repository.lib.ncsu.edu/handle/1840.16/9663 (accessed July 11, 2021).

[10] H.W. Yuchao Bai, C. Zhao, Y. Zhang, J. Chen, Additively manufactured CuCrZr alloy: Microstructure, mechanical properties and machinability, Mater. Sci. Eng. 819 (2021).

[11] Y. Danil, Pimenov, H. Ji, M.K. Gupta, Q. Song, W. Cai, T. Zheng, Y. Zhao, Z. Liu, Microstructure and machinability evaluation in micro milling of selective laser melted inconel 718 alloy, J. Mater. Res. Technol. (2021).

[12] A. Jiménez, P. Bidare, H. Hassanin, F. Tarlochan, S. Dimov, K. Essa, Powder-based laser hybrid additive manufacturing of metals: a review, Int. J. Adv. Manuf. Technol. 2021 1141. 114 (2021) 63–96. 10.1007/S00170-021-06855-4.

[13] W. Hintze, R. von Wenserski, S. Junghans, C. Möller, Finish machining of Ti6Al4V SLM components under consideration of thin walls and support structure removal, Procedia Manuf. 48 (2020) 485–491. 10.1016/J.PROMFG.2020.05.072.

[14] Meeting the Machining Challenges of Additive Manufacturing | Modern Machine Shop, (n.d.). https://www.mmsonline.com/articles/meeting-the-machining-challenges-of-additive-manufacturing (accessed October 15, 2021).

[15] P. Didier, G. Le Coz, G. Robin, P. Lohmuller, B. Piotrowski, A. Moufki, P. Laheurte, Consideration of SLM additive manufacturing supports on the stability of flexible structures in finish milling, J. Manuf. Process. 62 (2021) 213–220, https://doi.org/10.1016/J.JMAPRO.2020.12.027.

[16] G. Manogharan, R.A. Wysk, O.L.A. Harrysson, Additive manufacturing–integrated hybrid manufacturing and subtractive processes: economic model and analysis, Int. J. Comput. Integr. Manuf. 29 (5) (2016) 473–488, https://doi.org/10.1080/0951192X.2015.1067920.

[17] J.D. Perez Ruiz, S. Martinez Rodriguez, L. Norberto Lopez de la calle Marcaide, A. Lamikiz Mentxaka, H. Gonzalez Barrio, O. Pereira Neto, Un proceso robusto para el acabado en precisión de piezas fabricadas por impresión metálica,, Dyna - Ingeniería e industria 95 (2020) 436–442, https://doi.org/10.6036/9382.

[18] W.M. Tucho, P. Cuvillier, A. Sjolyst-Kverneland, V. Hansen, Microstructure and hardness studies of Inconel 718 manufactured by selective laser melting before and after solution heat treatment, Mater. Sci. Eng. A. 689 (2017) 220–232, https://doi.org/10.1016/j.msea.2017.02.062.

[19] P. Karimi, T. Raza, J. Andersson, L.-E. Svensson, Influence of laser exposure time and point distance on 75-μm-thick layer of selective laser melted Alloy 718, Int. J. Adv. Manuf. Technol. 94 (5-8) (2018) 2199–2207, https://doi.org/10.1007/s00170-017-1019-1.

[20] S.Y. Liu, H.Q. Li, C.X. Qin, R. Zong, X.Y. Fang, The effect of energy density on texture and mechanical anisotropy in selective laser melted Inconel 718, Mater. Des. 191 (2020), 108642, https://doi.org/10.1016/j.matdes.2020.108642.

[21] Z. Lei, J. Bi, Y. Chen, X. Chen, X. Qin, Z. Tian, Effect of energy density on formability, microstructure and micro-hardness of selective laser melted Sc- and Zr-modified 7075 aluminum alloy, Powder Technol. 356 (2019) 594–606, https://doi.org/10.1016/j.powtec.2019.08.082.

[22] J.H. Yi, J.W. Kang, T.J. Wang, X. Wang, Y.Y. Hu, T. Feng, Y.L. Feng, P.Y. Wu, Effect of laser energy density on the microstructure, mechanical properties, and deformation of Inconel 718 samples fabricated by selective laser melting, J. Alloys Compd. 786 (2019) 481–488, https://doi.org/10.1016/j.jallcom.2019.01.377.

[23] Z. Chen, S. Chen, Z. Wei, L. Zhang, P. Wei, B. Lu, S. Zhang, Y. Xiang, Anisotropy of nickel-based superalloy K418 fabricated by selective laser melting, Prog. Nat. Sci. Mater. Int. 28 (4) (2018) 496–504, https://doi.org/10.1016/j.pnsc.2018.07.001.

[24] S. Suwas, R.K. Ray, Texture Evolution During Solidification and Solid-State Transformation, in: Springer, London, 2014: pp. 73–93. 10.1007/978-1-4471-6314-5_4.

[25] G.P. Dinda, A.K. Dasgupta, J. Mazumder, Texture control during laser deposition of nickel-based superalloy, Scr. Mater. 67 (5) (2012) 503–506, https://doi.org/10.1016/j.scriptamat.2012.06.014.

[26] M.S. Pham, B. Dovgyy, P.A. Hooper, C.M. Gourlay, A. Piglione, The role of side-branching in microstructure development in laser powder-bed fusion, Nat. Commun. 11 (2020) 1–12, https://doi.org/10.1038/s41467-020-14453-3.

[27] Z. Liu, H. Qi, Effects of substrate crystallographic orientations on crystal growth and microstructure formation in laser powder deposition of nickel-based superalloy, Acta Mater. 87 (2015) 248–258, https://doi.org/10.1016/j.actamat.2014.12.046.

[28] M. Ni, C. Chen, X. Wang, P. Wang, R. Li, X. Zhang, K. Zhou, Anisotropic tensile behavior of in situ precipitation strengthened Inconel 718 fabricated by additive manufacturing, Mater. Sci. Eng. A. 701 (2017) 344–351, https://doi.org/10.1016/J.MSEA.2017.06.098.

[29] J.D. Pérez-Ruiz, L.N.L. de Lacalle, G. Urbikain, O. Pereira, S. Martínez, J. Bris, On the relationship between cutting forces and anisotropy features in the milling of LPBF Inconel 718 for near net shape parts, Int. J. Mach. Tools Manuf. 170 (2021), https://doi.org/10.1016/J.IJMACHTOOLS.2021.103801.

[30] M. Zhou, B.K.A. Ngoi, Effect of tool and workpiece anisotropy on microcutting processes, Proc. Inst. Mech. Eng. Part B J. Eng. Manuf. 215 (1) (2001) 13–19, https://doi.org/10.1243/0954405011515091.

[31] A.F. de Souza, K.S. Al-Rubaie, S. Marques, B. Zluhan, E.C. Santos, Effect of laser speed, layer thickness, and part position on the mechanical properties of maraging 300 parts manufactured by selective laser melting, Mater. Sci. Eng. A. 767 (2019), 138425, https://doi.org/10.1016/j.msea.2019.138425.

[32] T. Mishurova, S. Cabeza, T. Thiede, N. Nadammal, A. Kromm, M. Klaus, C. Genzel, C. Haberland, G. Bruno, The Influence of the Support Structure on Residual Stress and Distortion in SLM Inconel 718 Parts, Metall. Mater. Trans. A. 49 (7) (2018) 3038–3046, https://doi.org/10.1007/s11661-018-4653-9.

[33] L. Scime, J. Beuth, Anomaly detection and classification in a laser powder bed additive manufacturing process using a trained computer vision algorithm, Addit. Manuf. 19 (2018) 114–126, https://doi.org/10.1016/J.ADDMA.2017.11.009.

[34] P. Lott, H. Schleifenbaum, W. Meiners, K. Wissenbach, C. Hinke, J. Bültmann, Design of an Optical system for the In Situ Process Monitoring of Selective Laser Melting (SLM), Phys. Procedia. 12 (2011) 683–690, https://doi.org/10.1016/J.PHPRO.2011.03.085.

[35] S.K. Everton, M. Hirsch, P. Stravroulakis, R.K. Leach, A.T. Clare, Review of in-situ process monitoring and in-situ metrology for metal additive manufacturing, Mater. Des. 95 (2016) 431–445, https://doi.org/10.1016/J.MATDES.2016.01.099.

[36] . Serrano-Munoz, T. Mishurova, T. Thiede, M. Sprengel, A. Kromm, N. Nadammal, G. Nolze, R. Saliwan-Neumann, A. Evans, G. Bruno, The residual stress in as-built Laser Powder Bed Fusion IN718 alloy as a consequence of the scanning strategy induced microstructure, Sci. Reports 2020 101. 10 (2020) 1–15. 10.1038/s41598-020-71112-9.

[37] D. Wang, C. Yu, J. Ma, W. Liu, Z. Shen, Densification and crack suppression in selective laser melting of pure molybdenum, Mater. Des. 129 (2017) 44–52, https://doi.org/10.1016/j.matdes.2017.04.094.

[38] E. Budak, Mechanics and dynamics of thin walled structures, University of British Columbia 10.14288/1.0088030 (1994).

[39] Y. Kok, X.P. Tan, P. Wang, M.L.S. Nai, N.H. Loh, E. Liu, S.B. Tor, Anisotropy and heterogeneity of microstructure and mechanical properties in metal additive manufacturing: A critical review, Mater. Des. 139 (2018) 565–586, https://doi.org/10.1016/J.MATDES.2017.11.021.

[40] J.D. Pérez, H. Maury, J. Bris, M. Ojeda, Thermomechanical Modeling of a Sleeve Rehabilitation System for Pressure Pipes, J. Press. Vessel Technol. 142 (2020), https://doi.org/10.1115/1.4047443.

[41] F. Geiger, K. Kunze, T. Etter, Tailoring the texture of IN738LC processed by selective laser melting (SLM) by specific scanning strategies, Mater. Sci. Eng. A. 661 (2016) 240–246, https://doi.org/10.1016/J.MSEA.2016.03.036.